

Elastic–plastic–creep behavior of high rockfill dams: a case study on Lianghekou CRFD

Qiuting Jiang^{a,b}, Degao Zou^{a,b}, Jingmao Liu^{✉a,b}, Fanwei Ning^{a,b}, Kai Chen^{a,b}, and Wei Jin^c

^aThe State Key Laboratory of Coastal and Offshore Engineering, Dalian University of Technology, Dalian, Liaoning, 116024, China;

^bSchool of Hydraulic Engineering, Dalian University of Technology, Dalian, Liaoning, 116024, China; ^cChengdu Hydroelectric Investigation and Design Institute of Hydrochina, Chengdu, Sichuan, 610072, China

Corresponding author: **Jingmao Liu** (email: liujm@dlut.edu.cn)

Abstract

The instantaneous loading and time-dependent creep deformations occur simultaneously during the lifetime of rockfill dams, but their proportions in monitoring records are still unclear. In previous works, loading and creep were generally simulated independently in turn. This uncoupled method may induce misleading conclusions in interpreting dam behaviors. In this paper, an advanced elastic–plastic–creep model is applied to capture the interaction of loading and creep under complex conditions with varying loading rates based on a benchmark example of 295 m high Lianghekou core wall rockfill dam. The instantaneous elastic–plastic parameters of rockfills are calibrated by large-scale triaxial tests (including 300 and 800 mm in diameter) and the time-dependent creep parameters are obtained by back analyses on monitoring records. A series of numerical analyses on the dam are conducted. The loading–creep coupling process of rockfills is successfully captured and the instantaneous and time-dependent creep deformations are explicitly separated. The 800 mm diameter triaxial test weakens the size effect and provides an acceptable representation for the instantaneous behaviors of prototype rockfills. The good agreement between the calculations of the elastic–plastic–creep coupling analysis and measurements indicates creep contributes about 8%–15% to total construction deformation. The work provides guides for properly interpreting and evaluating actual dam behaviors.

Key words: dams, creep, rockfill, loading–creep coupling effect, size effect

Introduction

In recent decades, a large number of rockfill dams higher than 200 m and up to 300 m have been built and planned (Zhou et al. 2011; Xu et al. 2012; Wen et al. 2018), such as Nuozhadu core wall rockfill dam (CRFD) (261.5 m), Lianghekou CRFD (295 m), and Shuangjiangkou CRFD (314 m) in China. Compared with low dams, the instantaneous loading and time-dependent creep deformations of high rockfill dams are much more significant with high internal stresses (up to several megapascals). The difficulty of dam deformation control and the safety risk of anti-seepage control system increase significantly with dam height (Hunter and Fell 2003a, 2003b; Wen et al. 2017, 2018). Numerous surface cracks and high leakage rates have been observed in some in-service high rockfill dams due to excessive differential deformations (Cetin et al. 2000; Hunter and Fell 2003b; Lin et al. 2017), such as Ataturk CRFD (169 m), El Infiernillo CRFD (148 m), Cougar CRFD (159 m), and Pubugou CRFD (186 m). However, the roles of instantaneous loading and time-dependent creep deformations in these differential deformations are still unclear, which is unfavorable for dam safety assessment.

Actually, loading and creep occur simultaneously during the whole lifetime of a rockfill dam due to the dam construction, reservoir impoundment, and seasonal reservoir fluctuations. To reproduce the time-dependent creep deformation of high rockfill dams is a very difficult subject. The creep behavior of rockfills was often neglected in the early prediction works of dam deformation, results showing a significant underestimation of actual values (Naylor et al. 1997; Lollino et al. 2005). With the development of experimental techniques and computational methods, numerous experimental investigations and creep models have been developed to describe the time-dependent behavior of rockfills in recent years (Oldecop and Alonso 2007; Zhou et al. 2011; Fu et al. 2019). A large number of scholars (Zhou et al. 2011; Wen et al. 2017; Jia et al. 2018) have established the relationships between creep and stress state and time using empirical formulas to fit creep test curves under a single loading path, and applied them to engineering predictions. The calculation started by obtaining the instantaneous strains and stresses under the current loading increment by common numerical analysis techniques (for example, mid-point incremental method (Zhou et al. 2011; Wen et al. 2017)); then,

the incremental creep strains under the current stress condition and elapsed time were computed based on the empirical creep model used; finally, the virtual nodal forces equivalent to these incremental creep strains were applied and computed using initial strain method. The procedure has been extensively used in recent works (Fedà 1992; Zhou et al. 2011; Wen et al. 2017; Jia et al. 2018). The method is only approximate even if the numerical results showed good agreement with measurements, because it neglects the effect of loading history and the interaction of loading and creep. The multistage loading-creep tests on coarse-grained soils showed a clear strain-hardening phenomenon during post-creep loading (AnhDan et al. 2006; Zhang et al. 2017; Liu et al. 2023). This idea is not incorporated in these empirical creep models. The deviation of model theory from physical reality may lead to misinterpretation of monitoring records and control factors of dam damage.

The development and implementation of a more realistic constitutive model are required to take into account the complex stress-strain-time coupling relationship in rockfills. In recent years, the theoretical exercises of the constitutive model considering the elasticity, plasticity, and creep of geomaterials have made great progress based on multi-stage loading-creep tests (Fu et al. 2019; Yao and Fang 2020; Liu et al. 2023). The emphasis of such models is that the stress point initially at yield would fall into the expanded yield surface as the creep strain increases and the stress-strain curve during post-creep loading stage shows the hardening characteristic similar to unloading-reloading path. However, the application of these models in engineering is still very scarce. The creep model proposed by Liu et al. (2023) allows for reproducing the loading-creep coupling hardening behavior of rockfills under complex conditions (including monotonic and cyclic loading) with varying loading rates. The model can be easily implemented into the finite element calculation program by the modified Newton-Raphson method (Ma and May 1986). Therefore, the model is adopted in this study, seeing later Section "Unified Elastic-Plastic-Creep Model".

Besides the constitutive model adopted, the success of finite element simulation of rockfill dams depends on the model parameters. Coarse-grained soils with particle sizes ranging from 0.2 to 1.0 m have been widely used as dam shell rockfills (Varadarajan et al. 2006; Seo et al. 2009; Alonso et al. 2012). It is impossible to test prototype rockfills due to the physical limitations of laboratory equipment. In general, the rockfill specimens with reduced gradations, such as those with a maximum particle size between 40 and 80 mm, are tested to estimate the prototype properties (Varadarajan et al. 2006; Costa and Alonso 2009; Seo et al. 2009; Alonso et al. 2011; Mahinroosta et al. 2015; Zhou et al. 2018). The impact of particle size on rockfill behaviors has been investigated through laboratory tests of various size specimens (Marsal 1967, 1973; Marachi 1969; Marschi et al. 1972; Hu et al. 2011; Mahinroosta and Alizadeh 2012; Ovalle et al. 2014; Liu et al. 2021; Ning 2022), particle fracture-mechanics analysis (Frossard et al. 2012; Zhou et al. 2018), discrete-element method (Alonso et al. 2012), and empirical method (Hunter and Fell 2003a; Xu et al. 2012; Zou et al. 2013). These works have demonstrated the strong particle size dependence of

rockfill behaviors. Some scaling relations between rockfill behaviors (i.e., compressibility, shear strength, and fracture energy) and particle size have been developed. However, few of them are verified by in-situ measured data from practical engineering. Meanwhile, the influence degree of particle size on deformation and strength parameters varies among rockfills. How to eliminate the particle size effect in numerical simulation remains an open question.

The paper presents an application of the unified elastic-plastic creep model of Liu et al. (2023) in the 295 m high Lianghekou CRFD in China, currently the second-highest CRFD built in the world. The dam was well instrumented with a detailed monitoring system and massive continuous deformation records were obtained during construction and impoundment. Large-scale triaxial tests (including 800 and 300 mm in diameter) are conducted to model the particle size effect and calibrate the instantaneous elastic-plastic parameters of rockfills. Back analyses on monitoring records are conducted to calibrate the time-dependent creep parameters due to the poor representativeness of laboratory creep tests completed within several hours or days (Zhang et al. 2017; Zhu 2017). Then, a series of three-dimensional finite element analyses are performed to simulate the dam construction and impoundment. A separation of instantaneous and time-dependent creep deformations is made based on comparison studies between the calculations and measurements. Finally, the post-construction performance of the dam is predicted and discussed.

Lianghekou CRFD

General

Lianghekou CRFD is located in Yajiang County, Ganzi Prefecture, Sichuan Province, China, constructed for electricity generation and flood control. The power station's installed capacity is 3000 MW, with an annual energy output of 110 billion kW·h. The normal water level of the reservoir is 2865 m and the total storage capacity is 107.67 billion m³. The layout of the dam is shown in Fig. 1a. The dam has a height of 295 m and a bottom elevation of 2580 m, with a crest of 16 m width and 668 m length. The integrated upstream and downstream slopes are 1:2.0 and 1:1.9, respectively. The material zones are depicted in Fig. 1b. There are six material zones in total, including rockfill I, II, and III zones, transition, filter, and core wall. The dam shell rockfills (including rockfill I, II, and III zones, transition, and filter) are mainly composed of quarried slate and sandstone. The central core wall is composed of low-plasticity clayey gravels, with a slope of 1:0.2 on both up and downstream sides. The dam is built on bedrock and a grout curtain is designed to control foundation seepage. The slopes in left and right abutments are 1:1.3 and 1:1.1 above the elevation of 2725 m, respectively, and 1:0.9 below 2725 m, as shown in Fig. 1c.

Construction and impoundment schemes

The dam construction began in July 2016 and was completed in March 2022, nearly 6 years. The actual construction and impoundment schemes are presented in Fig. 2. The

Fig. 1. Lianghekou core wall rockfill dam (elevation in meters): (a) layout of dam; (b) maximum cross-section and layout of electromagnetism-type settlement gauges; and (c) maximum longitudinal section.

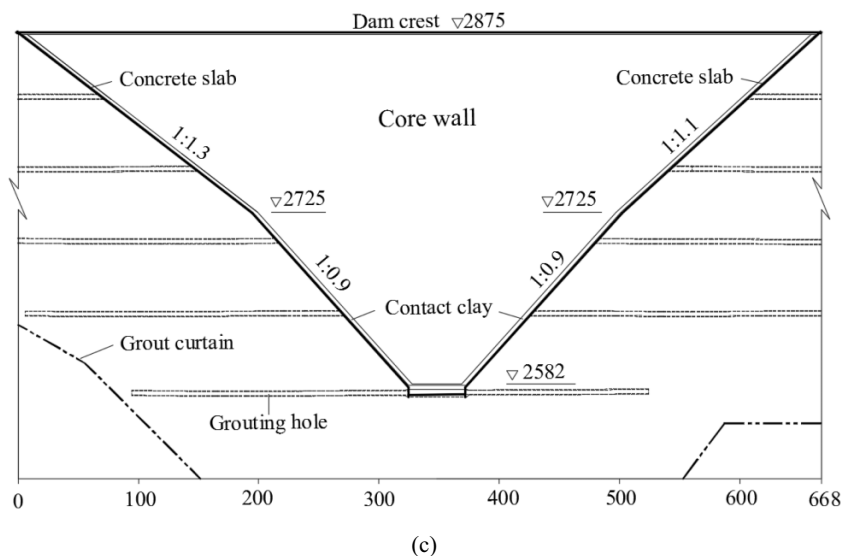
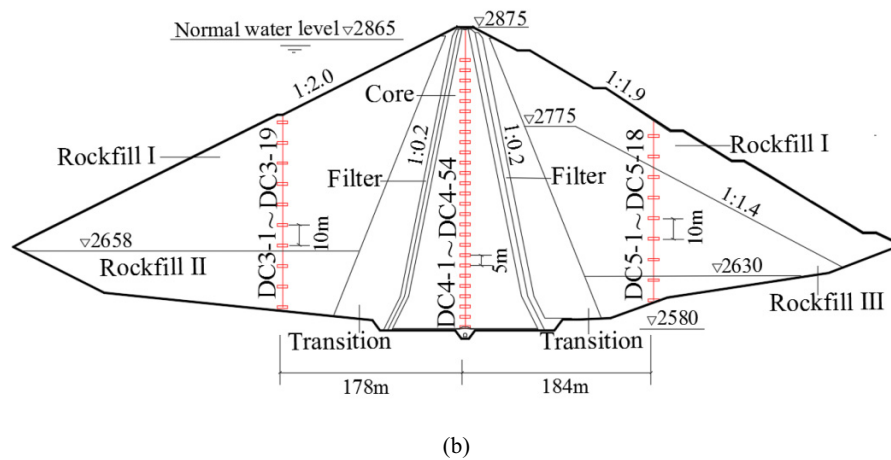
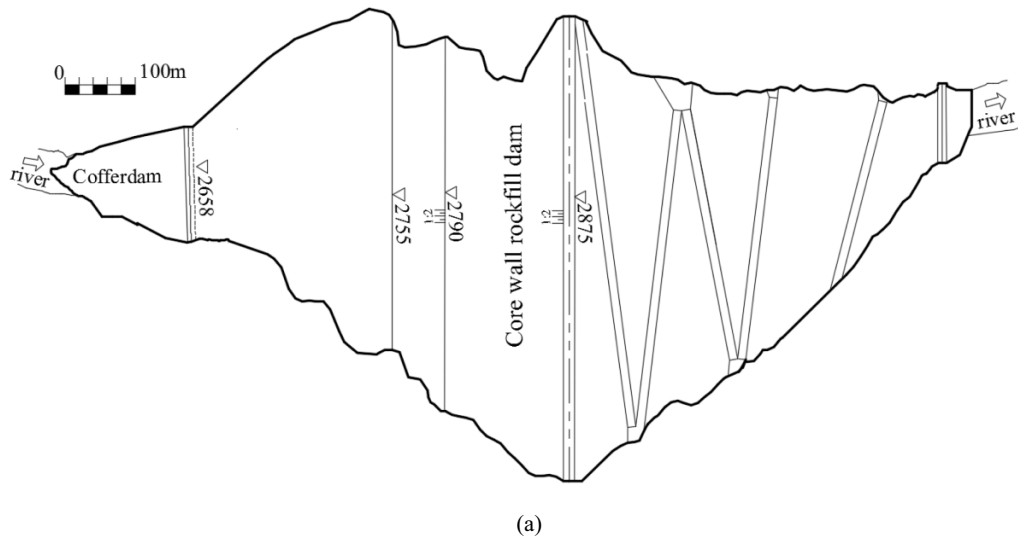
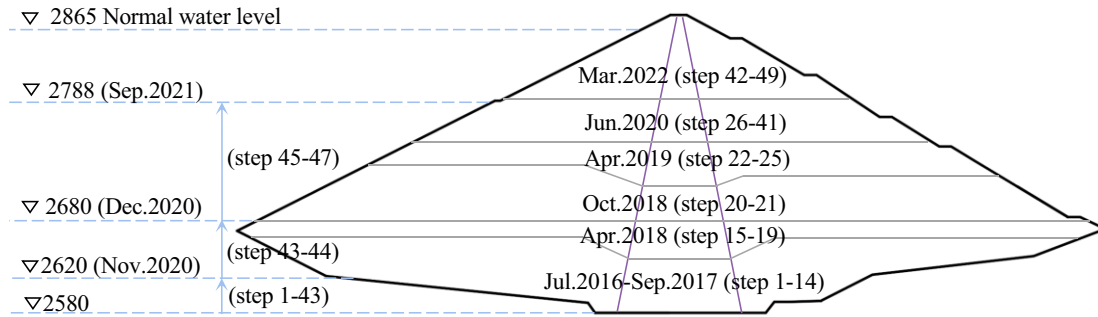


Fig. 2. The dam construction and impoundment processes (elevation in meters).



filling heights of different material zones differed before June 2020 but coincided after that. The water level remained below the elevation of 2620 m (0.14H, $H = 295$ m) before November 2020. Subsequently, the reservoir was rapidly impounded to 2680 m (0.34H) within the first 22 days of December 2020 and maintained the level for the next 5 months. The water level continued to rise to 2788 m from June to September 2021 and then remained stabilized until the dam completion.

Deformation monitoring system

A comprehensive and detailed monitoring system with numerous instrumentation has been established to track the dam behaviors. Electromagnetism-type settlement gauges, horizontal displacement gauges of tensional wire, and flexible inclinometers were installed in five cross-sections of the dam. The layout of 91 electromagnetism-type settlement gauges in the maximum cross-section (0 + 340 m) is shown in Fig. 1b. The three monitoring verticals of DC3 (upstream), DC4 (core), and DC5 (downstream) locating these gauges are 178, 0, and 184 m from the centreline of the cross-section, respectively. Eight horizontal displacement gauges of tensional wire (C60–C67) located at the elevation of 2675 m in the downstream shell of the maximum cross-section and 34 flexible inclinometers (IN-R5–IN-R7) at the elevation of 2760 m along the longitudinal axis of core wall are presented in the later Section "Results and Analyses".

Unified elastic-plastic-creep model

The constitutive model presented here adopts the unified elastic-plastic-creep model proposed by Liu et al. (2023). In the model, the total strain of soils is composed of recoverable elastic strain, instantaneous plastic strain, and time-dependent creep strain. The total strain-rate tensor is expressed as:

$$(1) \quad \dot{\epsilon} = \dot{\epsilon}^e + \dot{\epsilon}^p + \dot{\epsilon}^t$$

where the dot denotes rate in time or incremental quantity; the superscripts e and p denote the time-independent elastic and plastic components, respectively; the superscript t denotes the time-dependent creep component.

The constitutive relation is expressed as:

$$(2) \quad \dot{\sigma}' = \mathbf{D}_{ep} (\dot{\epsilon} - \dot{\epsilon}^t)$$

$$(3) \quad \mathbf{D}_{ep} = \mathbf{D}_e - \frac{\mathbf{D}_e \mathbf{n}_g \mathbf{n}^T \mathbf{D}_e}{h_{L/U}^p + \mathbf{n}^T \mathbf{D}_e \mathbf{n}_g}$$

where $\dot{\sigma}'$ is the effective stress rate tensor; \mathbf{D}_{ep} is the elastic-plastic stiffness tensor; \mathbf{D}_e is the elastic stiffness tensor; \mathbf{n} is the loading direction tensor; \mathbf{n}_g is the plastic flow direction tensor; and h^p is the plastic modulus. And loading and unloading are denoted by the subscripts L and U, respectively.

The criterion for distinguishing loading and unloading is as follows:

$$(4) \quad \begin{aligned} \mathbf{n}^T \dot{\sigma}' s_n &> 0 \text{ loading} \\ \mathbf{n}^T \dot{\sigma}' &= 0 \text{ neutral loading} \\ \mathbf{n}^T \dot{\sigma}' s_n &< 0 \text{ unloading} \end{aligned}$$

where $s_n = 1.0$ when $h^p \geq 0$ and $s_n = -1.0$ when $h^p < 0$.

The elastic shear and bulk moduli are expressed as

$$(5) \quad G = G_0 p_a \left(\frac{p'}{p_a} \right)^n$$

$$(6) \quad K = K_0 p_a \left(\frac{p'}{p_a} \right)^n$$

where G_0 , K_0 , and n are model constants; p_a is one atmospheric pressure; and p' is the mean effective stress.

The plastic flow direction tensor \mathbf{n}_g is expressed as

$$(7) \quad \mathbf{n}_g = \left(\frac{d}{\sqrt{1 + d_g^2}}, \frac{1}{\sqrt{1 + d_g^2}}, \frac{q M_g \sin 3\theta}{2\sqrt{1 + d_g^2}} \right)^T$$

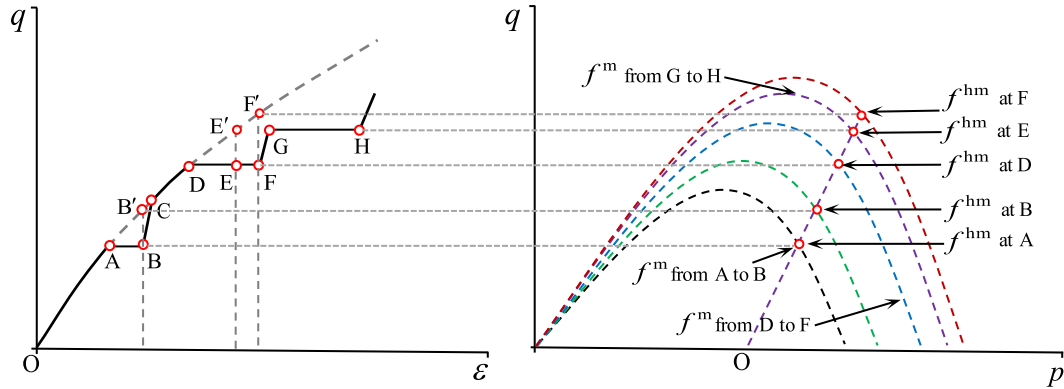
in which $d_g = (1 + \alpha_g) (M_g - \eta)$; $M_g = 6M_g^c / (7 + \sin 3\theta)$; θ is the stress Lode's angle; $\eta = q/p'$ is the current stress ratio; M_g^c and α_g are model constants; $d = d_g$ under virgin loading and reloading paths and $d = -|d_g|$ under the unloading path.

The loading direction tensor is expressed as

$$(8) \quad \mathbf{n} = \left(\frac{d_f}{\sqrt{1 + d_f^2}}, \frac{1}{\sqrt{1 + d_f^2}}, \frac{q M_f \sin 3\theta}{2\sqrt{1 + d_f^2}} \right)^T$$

in which $d_f = (1 + \alpha_f) (M_f - \eta)$; $M_f = 6M_f^c / (7 + \sin 3\theta)$; M_f^c and α_f are model constants.

Fig. 3. The evolution of yield surface during loading and creep.



The loading/reloading and unloading plastic moduli are, respectively, expressed as

$$(9) \quad h_L^p = h_0 p_a \left(\frac{p'}{p_a} \right)^m \left[1 - \frac{\alpha_f \eta}{(1 + \alpha_f) M_f} \right]^4 \times \left[1 - \frac{\eta}{M_g} + \beta_0 \beta_1 \exp(-\beta_0 \epsilon_s^{ir}) \right] \exp[\gamma_{dm} (1 - \chi)]$$

$$(10) \quad h_U^p = h_{u0} p_a \left(\frac{p'}{p_a} \right)^m \left(\frac{M_g}{\eta_u} \right)^{\gamma_u}$$

in which $\chi = (\eta - \eta_{un})/(\eta_{max} - \eta_{un})$ when $\eta > \eta_{un}$, and $\chi = ((\eta - \eta_r)/(\eta_{um} - \eta_{un})) / ((\eta_{um} - \eta_r)/(\eta_{max} - \eta_{un}))$ when $\eta \leq \eta_{un}$; η_{max} , η_{um} , η_{un} , and η_r are the stress ratios at the maximum hardening state, maximum reverse reloading-unloading stress state inside maximum stress state, latest reverse unloading-reloading stress state, and maximum unloading stress state, respectively; $\epsilon_s^{ir} = \int (d\epsilon_s^p + d\epsilon_s^t)$ is the sum of plastic and creep deviatoric strains; h_0 , h_{u0} , m , β_0 , β_1 , γ_{dm} , γ_u are model constants.

The creep strain-rate tensor can be divided into the volumetric and deviatoric components

$$(11) \quad \dot{\epsilon}^t = \dot{\epsilon}_v^t \frac{\partial p}{\partial \sigma} + \dot{\epsilon}_s^t \frac{\partial q}{\partial \sigma}$$

The volumetric and deviatoric creep strain rate expressions are as follows:

$$(12) \quad \dot{\epsilon}_v^t = \alpha_v \epsilon_{vf}^t \left(1 - \frac{\epsilon_{vc}^t}{\epsilon_{vf}^t} \right)^c$$

$$(13) \quad \dot{\epsilon}_s^t = \alpha_s \epsilon_{sf}^t \left(1 - \frac{\epsilon_{sc}^t}{\epsilon_{sf}^t} \right)^c$$

in which α_v and α_s are the initial slopes between the creep strains and time; c is the model constant.

The final volumetric and deviatoric creep strains are as follows:

$$(14) \quad \epsilon_{vf}^t = c_1 \left(\frac{p'}{p_a} \right)^{m_1}$$

$$(15) \quad \epsilon_{sf}^t = c_2 \left(\frac{p'}{p_a} \right)^{m_2} \eta^{m_3}$$

in which c_1 , c_2 , m_1 , m_2 , and m_3 are model constants.

The cumulative creep strain $\epsilon_c^t [\epsilon_{vc}^t, \epsilon_{sc}^t]$ expression is as follows:

$$(16) \quad \epsilon_c^t = \epsilon_c^{hm} - \epsilon_c^{it}$$

$$(17) \quad \epsilon_c^{it} = \begin{cases} \epsilon_c^{hm} - \frac{p_c^{hm} - p_c}{p_c^{hm} - p_c^m} (\epsilon_c^{hm} - \epsilon_c^m) & p_c > p_c^m \\ \epsilon_c^m & p_c \leq p_c^m \end{cases}$$

in which p_c is the current stress state; p_c^m is the maximum stress state under virgin loading corresponding to the size of the yield surface f^m ; p_c^{hm} is the maximum hardening state under current loading condition (monotonic, cyclic, or creep loading) corresponding to the size of the yield surface f^{hm} ; ϵ_c^{hm} is the current strain; ϵ_c^{it} is the strain in the virgin loading curve at the current stress state; ϵ_c^m is the inelastic strain corresponding to f^m in the virgin loading curve. Considering the loading path A-B-C-D-E-F-G-H in Fig. 3 as an example, the yield surface f^m is constant during creep (such as $A \rightarrow B$, $D \rightarrow F$, and $G \rightarrow H$) and varies with stress during loading (such as $O \rightarrow A$, $B \rightarrow D$, and $F \rightarrow G$), while the yield surface f^{hm} varies with time (such as $A \rightarrow B$, $D \rightarrow F$, and $G \rightarrow H$). If the current stress state is at point G, ϵ_c^{hm} is the strain at point G, ϵ_c^{it} is the strain at point E', and ϵ_c^m is the strain obtained by eq. 17 with the stress state at point E'.

Advanced models that consider salient features of soil behaviors under cyclic or creep loading seem to require more parameters (Ling and Liu 2003; Ling and Yang 2006; Fu et al. 2019). In the present model, eleven constants are required to describe the instantaneous elastic-plastic behaviors of rock-fills under monotonic loading, including elastic constants G_0 , K_0 , and n , plastic flow direction constants α_g and M_g^c , loading direction constants α_f and M_f^c , and plastic modulus constants h_0 , m , β_0 , β_1 , and three more plastic modulus constants γ_{dm} , h_{u0} , γ_u are required under cyclic loading. Seven more constants are needed to describe the creep behavior, including volumetric creep constants α_v , c_1 , m_1 and deviatoric creep constants α_s , c_2 , m_2 , m_3 . These instantaneous elastic-plastic parameters are calibrated by triaxial tests following the procedure of Liu et al. (2023). The time-dependent creep parameters are obtained by back analyses on monitoring records due to the poor representativeness of

Table 1. Equipment parameters of super large-scale and large-scale triaxial devices.

Devices	Large-scale triaxial test	Super large-scale triaxial test
Specimen size (diameter×height, mm×mm)	300×700	800×1760
Maximum particle size (mm)	60	160
Maximum axial force (kN)	1500	10 000
Maximum axial displacement (mm)	150	500
Maximum confining pressure (MPa)	4	3

creep tests completed within several hours or days (Zhang et al. 2017; Zhu 2017). Details have been described in the next section.

Material parameters

Instantaneous elastic–plastic parameters

Two different sizes of large-scale triaxial devices in the Earthquake Engineering Research Institute of Dalian University of Technology are used to test the dam shell rockfills to model the particle size effect and identify their mechanical properties. The equipment required to test the specimen of 300 mm in diameter and 700 mm in height is called large-scale triaxial device and the equipment required to test the specimen of 800 mm in diameter and 1760 mm in height is called super large-scale triaxial device. These two triaxial devices are capable of producing maximum axial forces of 1500 and 10 000 kN, respectively, and maximum confining pressures of 4 and 3 MPa, respectively. The equipment parameters of super large-scale and large-scale triaxial devices are listed in Table 1. More details can be found in Ning (2022).

Previous experimental studies showed that the loading rate in constant strain rate tests has little effect on the stress–strain relations of gravelly soils (AnhDan et al. 2006; Lade et al. 2009; Liu et al. 2023). Hence, it is believed that only the instantaneous deformation due to loading occurs during the tests. The rockfill from the rockfill I zone is tested here at 0.5, 1.5, and 2.5 MPa confining pressures and the experiments are conducted at the strain rate of 0.1%/min. The laboratory specimens are prepared at standard test methods for soils in China (CS 2019). The gradations of the specimens are scaled down to be parallel to the prototype gradation curve, as shown in Fig. 4. The scale ratio in maximum particle size is 10 and 3.75 for the 300 and 800 mm diameter specimens, respectively. The ratio of specimen diameter to maximum particle size remains 5 (Marachi 1969; Xiao et al. 2015; CS 2019). The initial porosity for all specimens is 21%, which is consistent with the prototype.

The deviatoric stress–axial strain–volumetric strain curves from these two different sizes of triaxial tests are shown in Figs. 5a and 5b. Within the general stress level of dam, the stress–strain curves of 300 mm diameter specimen show higher secant modulus and lower compressibility than the 800 mm diameter specimen. The volumetric strain for the large-size specimen at a given stress condition is appreciably larger than that for the small-size specimen. This can be explained by the dependence of particle breakage on particle

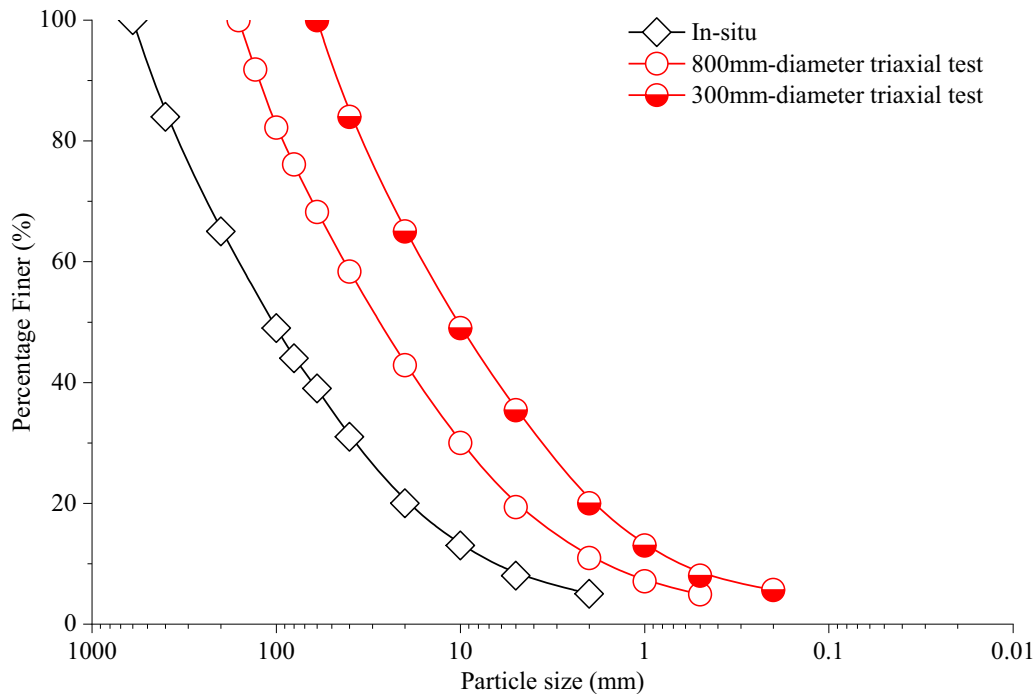
size (Xiao et al. 2020a; Ning 2022). The increase of particle breakage ratio with particle size leads to an increase in the content of fine particles and the volume of specimens shrinks significantly when the pores between particles are filled (Xiao and Liu 2017; Xiao et al. 2020b).

Two suites of instantaneous elastic–plastic parameters for the rockfill are calibrated from the experimental results, called large-scale triaxial test parameters (LTP) and super large-scale triaxial test parameters (SLTP), as shown in Table 2. The elastic constants G_0 and K_0 in LTP are slightly smaller and larger than those in SLTP, respectively. The difference of the two suites parameters mainly lies in the plastic parameters, which dominate the particle size effect on rockfill behaviors. For example, the value of h_0 of the 300 mm diameter specimen is three times that of the 800 mm diameter specimen, indicating a much lower plastic modulus of 800 mm diameter specimen. The same critical stress ratio M_g^c from the two different sizes of specimens is obtained.

Figs. 5a and 5b compare the deviatoric stress–axial strain–volumetric strain curves from the two sizes of specimens with the curves simulated using the parameters. The model reproduces well the general trend of these experimental curves at different confining pressures. The same instantaneous elastic–plastic parameters as the rockfill I zone are assumed for all dam shell rockfills due to the similar physical properties of rockfill I, II, and III zones and the small filling volume of filter and transition. The dry density of rockfill I, II, III zones is 2250, 2230, and 2230 kg/m³, respectively, and their in-situ gradation curves have a maximum difference of only 3%.

Previous experimental study showed that the maximum particle size of coarse particles has a minor impact on the strength and deformation characteristics of core-wall materials when the percentage of fine particles smaller than 5 mm is more than 50% (the coarse particles are suspended among fine particles, failing to form a skeleton) (Zuo et al. 2020). Therefore, the instantaneous elastic–plastic parameters of core-wall material of Lianghekou dam are calibrated through a set of 100 mm diameter triaxial tests (Li 2015), also shown in Table 2. The simulated results using the parameters are given in Fig. 6, showing a similar trend to the experimental curves. In the simulation of core wall, the strategy incorporating porosity and saturation into the undrained method of Naylor (1974) is applied to consider the compression of pore fluid (Fredlund 1976). The measured porosity of 18.8% and degree of saturation following the normal distribution with a mean of 88% and variance of 0.001 at compaction of core

Fig. 4. Gradation curves of the rockfill from rockfill I zone.



wall are introduced as input data for analysis, as in Zou et al. (2022).

Time-dependent creep parameters

Comparison of laboratory creep tests and field monitoring data (Sowers 1965; Oldecop and Alonso 2007; Zhang et al. 2017; Zhu 2017; Liu et al. 2023) shows that it takes only a few days for the creep strain to be stable in a laboratory rockfill specimen, while it need take a few years in an actual rockfill dam. It is impractical to characterize the time-dependent behavior of rockfill dams through laboratory creep tests. Therefore, back analysis on monitoring data to identify time-dependent creep parameters has been widely adopted. Early studies provided the range of relevant coefficients of empirical equations by fitting the linear relationships between post-construction settlement and logarithm of time (Sowers 1965; Clements 1984; Maranha das Neves 1991). With the development of viscoelastic models for soils, many parameter identification procedures were proposed (Ohkami and Swoboda 1999; Guo 2000; Yang et al. 2001), for example, the method using the elastic-viscoelastic correspondence principle and the trial calculation method. In recent years, a multitude of intelligent algorithms (particle swarm optimization (PSO), neural networks, etc.) have been developed and applied to the back analyses of complex constitutive models (Zhou et al. 2011; Kong et al. 2016; Wen et al. 2017). The idea of the approaches is to transform the parameter identification problem into an optimization problem of an objective function by mathematical programming techniques of error minimization.

In this paper, the back-analysis method using the PSO algorithm developed by Kong et al. (2016) is used. The time-dependent creep parameters of the rockfill I zone and core

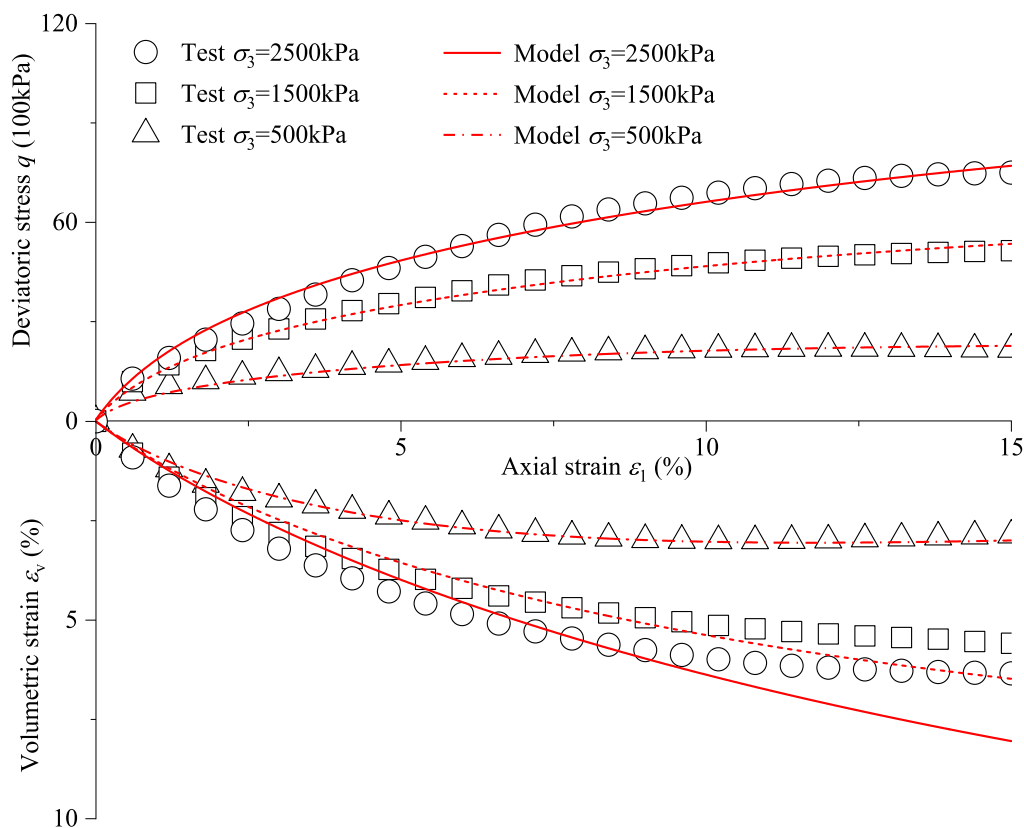
wall are inverted based on the field monitoring records from the electromagnetism-type settlement gauges DC5-18 and DC4-44. Likewise, the same time-dependent creep parameters as the rockfill I zone are adopted for all of the dam shell rockfills. For simplification, it is assumed based on previous researches (Jia et al. 2018; Zhang et al. 2004) that the creep strain rate (eqs. 12 and 13) is a linear function of remaining creep strain (i.e., $c = 1$) and the volumetric and deviatoric creep strain rate parameters are the same (i.e., $\alpha_v = \alpha_s$). The volumetric creep strain of core wall is assumed to be zero due to the core wall approaching undrained conditions with a high average degree of saturation 88% (Hunter and Fell 2003b).

On the other hand, the creep strain rate parameters (i.e., α_v and α_s) from previous back analyses on many in-service rockfill dams were found to be about two orders of magnitude smaller than those from laboratory tests (Zhu 2017; Jia et al. 2018; Liu et al. 2023). Meanwhile, the increase rate of final creep strain with mean effective stress decreases when the magnitude of pre-creep loading is large enough (Zhu 2017), which indicates that the exponential parameters m_1 and m_2 in eqs. 14 and 15 must be less than 1. Based on these works, a rough range of the parameters can be obtained: α_v and α_s : 0.0001–0.01; m_1 and m_2 : 0.1–1; m_3 : 0–5; c_1 and c_2 : 0.0001–0.01. The time-dependent creep parameters of the Lianghekou dam materials back-analyzed are listed in Table 2.

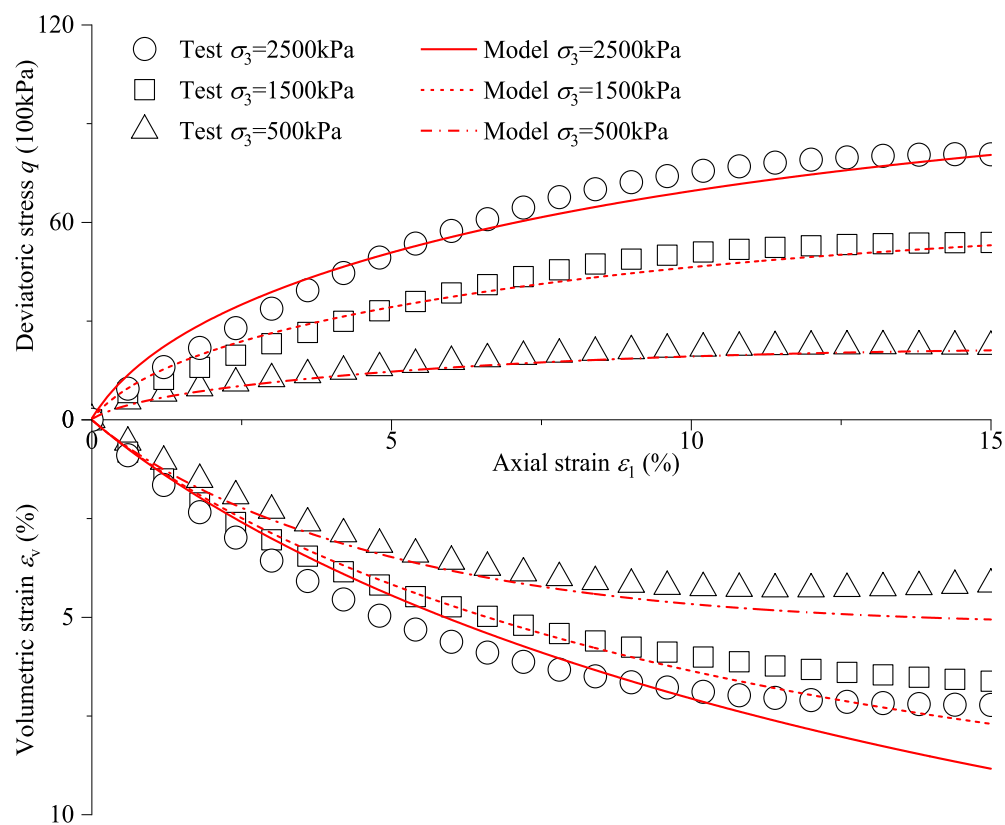
Finite element model

A three-dimensional finite element model including 57 754 elements and 61 230 nodes is established here to simulate the Lianghekou dam behaviors, as shown in Fig. 7. Two

Fig. 5. Triaxial tests on the rockfill from rockfill I zone: (a) large-scale triaxial test (300 mm in diameter) and (b) super large-scale triaxial test (800 mm in diameter).



(a)



(b)

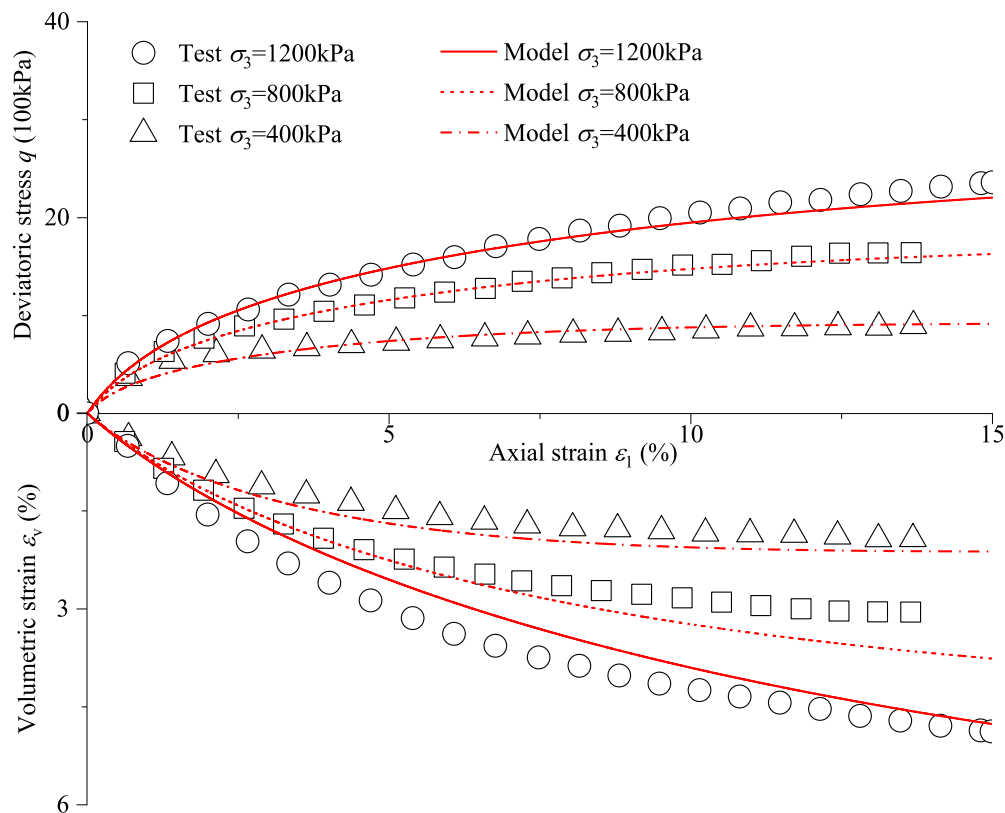
Table 2. Model parameters used for Lianghekou core wall rockfill dam.

Symbol	Instantaneous elastic-plastic parameters (triaxial tests)			Time-dependent creep parameters (back analyses)		
	Core wall	Dam shells		Symbol	Core wall	Dam shells
	100 mm diameter	300 mm diameter (LTP ^a)	800 mm diameter (SLTP ^b)			
G_0	780	2000	2145	$\alpha_s (10^{-3})$	9.93	9.23
K_0	800	2300	2200	$\alpha_v (10^{-3})$	–	9.23
M_g^c	1.30	1.78	1.78	$c_1 (10^{-3})$	0.00	0.27
M_f^c	1.00	1.65	1.20	$c_2 (10^{-3})$	0.11	0.26
α_f	0.25	0.15	0.18	m_1	–	0.51
α_g	–0.10	0.20	0.45	m_2	0.15	0.31
h_0	500	600	200	m_3	0.45	1.29
h_{u0}	500	3000	1000			
n	0.50	0.50	0.50			
m	0.30	0.27	0.60			
γ_{dm}	15	10	10			
γ_u	3.50	5	7			
β_0	20	12	20			
β_1	0.01	0.02	0.02			
n_0^c	18.80%	–	–			
S_0^d	N (88%, 0.001)	–	–			

^aLTP: large-scale triaxial test parameters.

^bSLTP: super large-scale triaxial test parameters. ^c n_0 : initial porosity. ^d S_0 : initial degree of saturation.

Fig. 6. Triaxial tests on core wall material of gravel clay (Li 2015).



element types, the isoparametric element and the proportional boundary polyhedron element (Chen et al. 2018, 2023) with a maximum size of 10 m, are employed in the model. The displacements (including horizontal and vertical dis-

placements) are fixed to zero at the dam bottom. Fig. 2 presents the dam construction and impoundment processes. The simulation of construction is completed in 49 steps by sequentially adding layers to the initial geometry of the dam

Fig. 7. Finite element model of Lianghekou dam.

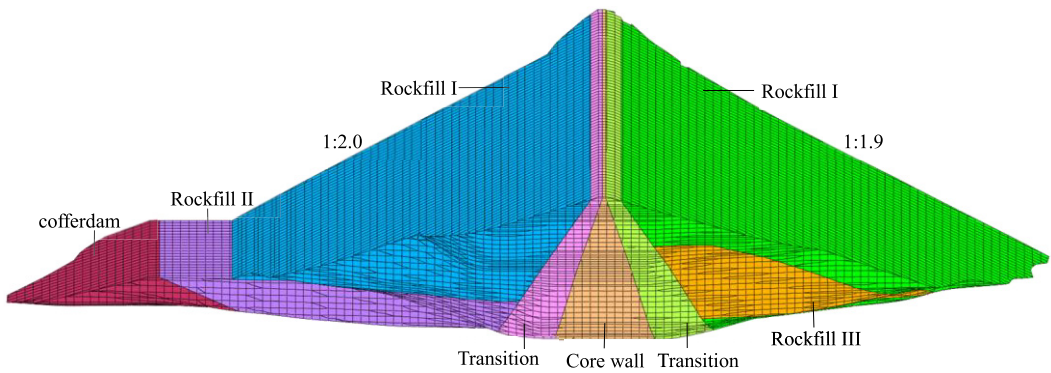


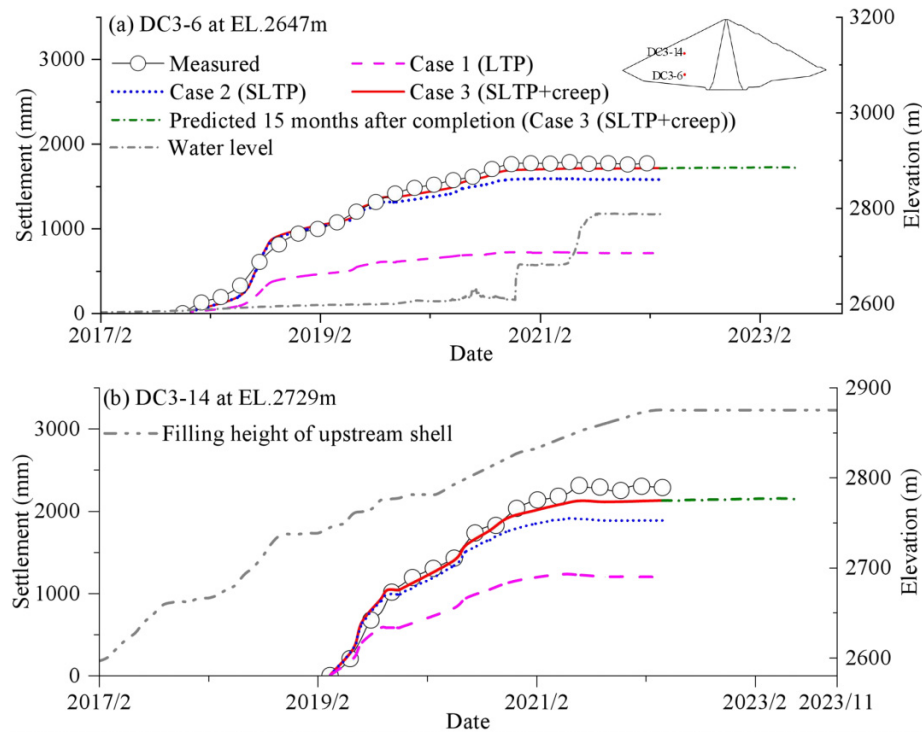
Table 3. Construction stages of Lianghekou dam.

Date	Elevation (m)	Loading step	Elapsed time (days)	Reservoir water level
July to October 2016	2585	1–9	122	
November 2016 to January 2017	2595	10–11	92	
February to March 2017	2605	12	59	
April to June 2017	2615	13	92	
July to August 2017	2625	14	61	
September 2017	2635	15	31	
October 2017	2645	16	30	
November to December 2017	2655	17	61	
January to February 2018	2665	18	62	
March 2018	2675	19	28	
April to June 2018	2685	20	92	
July to September 2018	2695	21	92	Remaining at 2620 m
October 2018	2705	22	30	
November 2018 to January 2019	2715	23	92	
February 2019	2725	24	31	
March 2019	2735	25	28	
April to July 2019	2745	26	122	
August to September 2019	2755	27	62	
October 2019	2765	28	30	
November 2019 to January 2020	2775	29–37	92	
February to March 2020	2785	38–40	60	
April to June 2020	2795	41	92	
July to September 2020	2805	42	92	
October 2020	2815	43	30	
November 2020 to January 2021	2825	44	92	Rising to 2680 m
February to March 2021	2835	45	59	Remaining at 2680 m
April to June 2021	2845	46	92	
July to September 2021	2855	47	92	Rising to 2788 m
October to December 2021	2865	48	91	Remaining at 2788 m
January to March 2022	2875	49	90	

in a ramp loading manner. Simultaneously, the reservoir is impounded to the water level 2788 m in the first 47 steps by imposing hydrostatic pressure on the upstream face of core wall and then keeps stable until the dam completion. The elapsed time of each step is determined by the field construction and impoundment schemes and the time increment is 10–30 days in the process of incremental solution. The

nonlinear finite element analysis program GEODYNA (Zou et al. 2005, 2013; Xu et al. 2016), developed by Earthquake Engineering Research Institute, Dalian University of Technology, is used in calculations. The dam construction process and the setting of the corresponding loading steps and the elapsed time of each step in GEODYNA are presented in Table 3.

Fig. 8. Settlement time histories in the upstream shell of cross-section 0 + 340 m (LTP: large-scale triaxial test parameters; SLTP: super large-scale triaxial test parameters): (a) DC3-6 at EL.2647 m and (b) DC3-14 at EL.2729 m.



Results and analyses

The model performance and dam behavior are compared based on the observation data. The maximum cross-section (0 + 340 m) equipped with more gauges than others is selected as the focus of investigation. The longest displacement time series available is from December 2016 to March 2022, covering the whole construction period.

Size effect

Two separate FE simulations are conducted to investigate the influence of size effect using the LTP and SLTP for dam shell rockfills in Table 2, known as Case 1 (LTP) and Case 2 (SLTP). The creep of all dam materials is assumed to be zero in this part, which has been executed by turning off the creep strain rate (i.e., $\alpha_s = \alpha_v = 0$ in eqs. 12 and 13).

The vertical and horizontal displacements of field records and FE simulations within 2650–2750 m elevations inside the dam shells of the maximum cross-section are plotted in Figs. 8–10. The filling process of upstream shell and the reservoir impounding process are also given in Fig. 8. These monitoring records provide a fairly clear description of accumulation process of the dam deformation with time. The continuous rise of filling height resulted in a large growth rate of measurements during construction. The measured settlements of the upstream shell (Fig. 8) were significantly affected by the reservoir impoundment and tended to stabilize after the monitoring gauges were flooded. However, the vertical and horizontal displacement growth rates simulated in Case

1 (LTP) (pink dash line) are significantly smaller than measurements, resulting in a considerable underestimation in displacement values. By contrast, the FE simulation in Case 2 (SLTP) (blue dot line) captures the evolution of measurements better although some divergence between them approximately after November 2019 is presented (which is related to the creep effect of rockfills and will be confirmed in the next part).

Figs. 11a and 11b compare the settlement distributions simulated and measured in the dam shells at completion (March 2022). Due to insufficient monitoring data, Fig. 12 only shows the horizontal displacement distribution at the elevation of 2675 m in the downstream shell in August 2021. The FE simulations in Case 1 (LTP) and Case 2 (SLTP) both capture these general distribution rules of measurements, for example, the bow-shaped settlement distribution along the dam height and the overall trend of horizontal displacement. However, the simulation in Case 2 (SLTP) shows a better agreement with measurements in magnitude. Table 4 gives the maximum settlements simulated and measured in different zones at completion. The underestimation in the maximum settlements of dam shells drops from 43%–45% to 12%–13% from Case 1 (LTP) to Case 2 (SLTP). The change in dam shell material parameters also induces some improvements (about 15%) in the settlement prediction of core wall, as shown in Figs. 11c and 13 and Table 4.

In summary, the rockfill dam behaviors present strong dependence on rockfill particle size and the size effect is clearly shown. The excessive scaling down of particle size

Fig. 9. Settlement time histories in the downstream shell of cross-section 0 + 340 m: (a) DC5-7 at EL.2651 m and (b) DC5-12 at EL.2702 m. LTP, large-scale triaxial test parameters; SLTP, super large-scale triaxial test parameters.

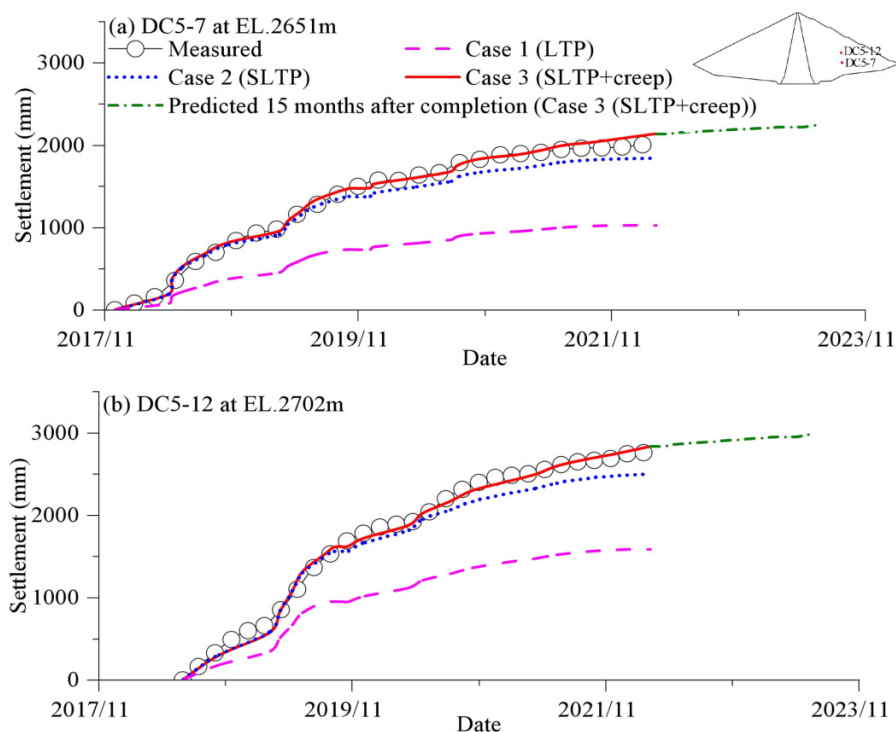


Fig. 10. Horizontal displacement time histories in the downstream shell of cross-section 0 + 340 m: (a) C64 at EL.2675 m and (b) C50 at EL.2745 m. LTP, large-scale triaxial test parameters; SLTP, super large-scale triaxial test parameters.

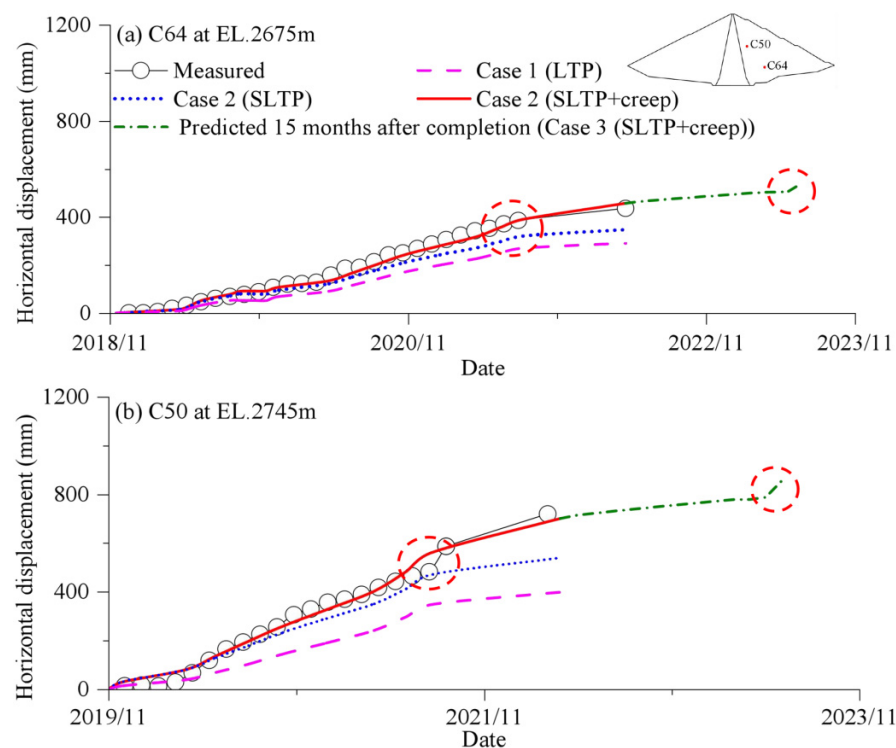
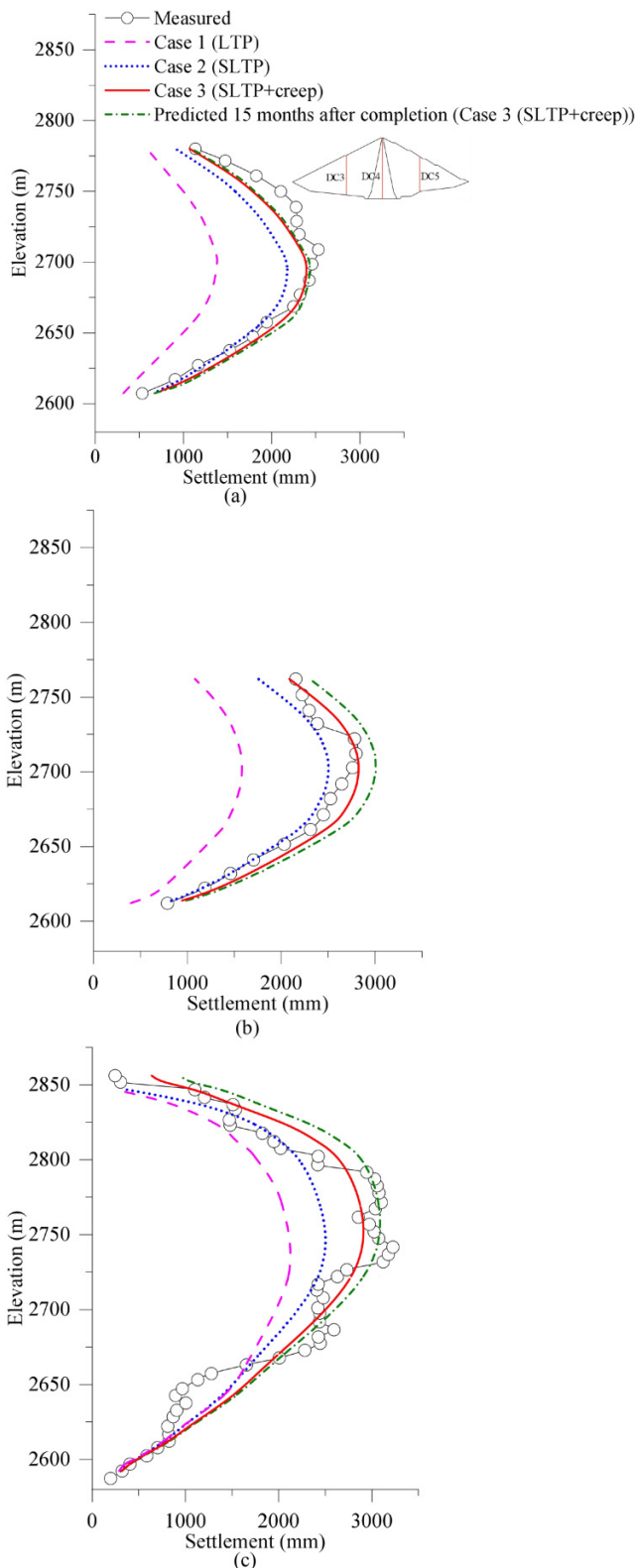


Fig. 11. Distributions of settlements in different material zones of cross-section 0 + 340 m at completion: (a) DC3 in the upstream shell; (b) DC5 in the downstream shell; and (c) DC4 in the core wall. LTP, large-scale triaxial test parameters; SLTP, super large-scale triaxial test parameters.



during the 300 mm diameter triaxial test has led to a severe underestimation in dam performance. The parameters provided by the 800 mm diameter triaxial test are able to characterize the instantaneous behaviors of prototype rockfills within an acceptable range, especially in the early stage of filling.

Time effect

Creep is an important time-dependent feature of rock-fill dams. On the basis of the above analyses, the SLTP for dam shell rockfills and time-dependent creep parameters in Table 2 are used in the following FE numerical simulation (Case 3 (SLTP + creep) for short). The construction displacement time histories simulated in this case are also presented in Figs. 8–10 and Fig. 11. Compared with Case 2 (SLTP), the FE simulation in Case 3 (SLTP + creep) (red solid line) shows a superior agreement with the evolution of measurements. The simulated displacements under these two cases develop consistently during the early stage of filling (approximately prior to November 2019 for the monitoring points shown in the figures) but divert more and more as the filling height continues to rise. It can be explained by the loading-creep coupling mechanisms. Although the stress state remains constant during creep, the increase of creep strain will induce an expanded yield surface (i.e., strain hardening effect) (Zhang et al. 2017). If the stress state during post-creep loading catches up with the expanded yield surface, the influence of previous cumulative creep strain is eliminated; if not, the creep strain continues to be accumulated. The process has been described by the two hardening state variables p_c^m and p_c^{hm} in the model of Section “Unified Elastic-Plastic-Creep Model”. From eqs. 16 and 17, when $p_c^m = p_c^{hm}$, the expanded yield surface is caught up and the cumulative creep strain is reset to zero, as the point C in Fig. 3. When $p_c^m < p_c^{hm}$, the accumulation of creep strain depends on the distance between the corresponding yield surfaces f^m and f^{hm} , as the distance between point E' and point G in Fig. 3.

The element A at the elevation of 2680 m in the downstream shell of Lianghekou dam in Fig. 12 is considered to be an example to illustrate the process. Fig. 12 shows the evolutions of $(p_c^{hm} - p_c^m)$ and rockfill placement rate with time. The rockfill placement rate is given to represent the magnitude of filling load increment and elapsed time. During the construction period, the oscillations of $(p_c^{hm} - p_c^m)$ show a clear negative correlation with the placement rate, i.e., the increase of placement rate followed by the decrease of $(p_c^{hm} - p_c^m)$. In the early stage of filling (before June 2020), the value of $(p_c^{hm} - p_c^m)$ sometimes decreases to zero when large filling load increment is imposed. In the late stage, the $(p_c^{hm} - p_c^m)$ is always greater than zero because of the longer filling period (as indicated by the decreasing trend of placement rate) and the smaller filling load increment due to dam geometry. After completion, p_c^m remains nearly constant and $(p_c^{hm} - p_c^m)$ grows smoothly. The example visualizes the interaction of loading and creep of rockfills and reproduces the accumulation process of creep.

Table 4. The maximum settlements measured and simulated at completion (unit: mm).

Locations	Case 1 (LTP)	Case 2 (SLTP)	Case 3 (SLTP + creep)	Measurements
Upstream (DC3)	1382 (45%)*	2198 (13%)*	2415 (5%)*	2531
Core wall (DC4)	2106 (35%)*	2582 (20%)*	2952 (8%)*	3228
Downstream (DC5)	1587 (43%)*	2510 (12%)*	2833 (−1%)*	2801

Note: LTP, large-scale triaxial test parameter; SLTP, super large-scale triaxial test parameter. * The difference of the settlements measured and simulated is in brackets.

Fig. 12. Distribution of horizontal displacements at 2675 m in August 2021 (positive horizontal displacement is downstream). LTP, large-scale triaxial test parameters; SLTP, super large-scale triaxial test parameters.

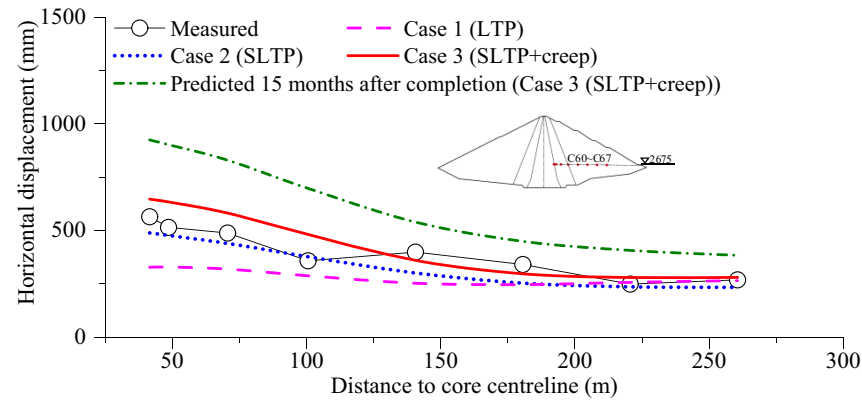
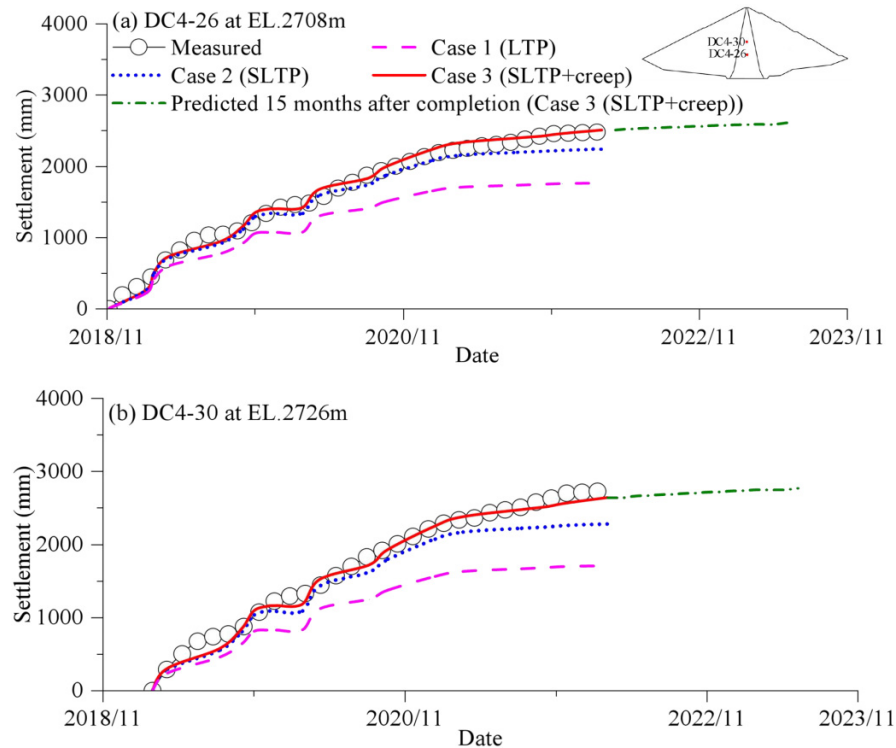


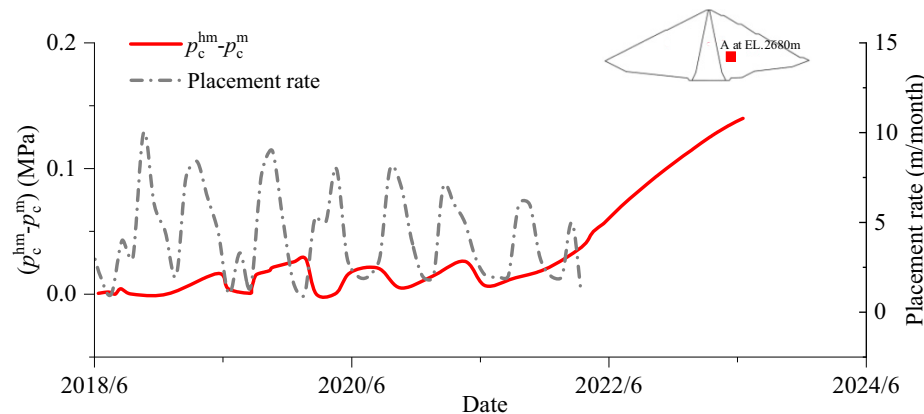
Fig. 13. Settlement time histories in the core wall of cross-section 0 + 340 m: (a) DC4-26 at EL.2708 m and (b) DC4-30 at EL.2726 m. LTP, large-scale triaxial test parameters; SLTP, super large-scale triaxial test parameters.



The process is consistent with the divergence in the displacement evolutions in Case 2 (SLTP) and Case 3 (SLTP + creep) in Figs. 8–10 and Fig. 11.

The simulated vertical and horizontal displacement distributions in Case 3 (SLTP + creep) at completion are also presented in Fig. 13 and 14. Moreover, the settlement

Fig. 14. The evolutions of $(p_c^{hm}-p_c^m)$ and rockfill placement rate in Lianghekou dam.



distributions at the elevation of 2760 m along the longitudinal axis of core wall under Case 2 (SLTP) and Case 3 (SLTP + creep) are compared with measurements in Fig. 15. As expected, a significant improvement in consistency between the FE simulation in Case 3 (SLTP + creep) and measurements is found compared with Case 2 (SLTP). Similarly, the maximum settlements in different zones of the dam at completion under Case 3 (SLTP + creep) are also given in Table 4. The underestimation in maximum measured settlements drops from 12%–20% to 1%–8% from Case 2 (SLTP) to Case 3 (SLTP + creep). The difference in the settlements under the two cases indicates the contribution of creep in total construction settlement, about 8%–15%. It is worth mentioning that the underestimation of the settlements in the upstream shell is somewhat larger than that in the downstream shell since no collapse settlement during impounding is modeled in the present work.

Overall, the Case 3 (SLTP + creep) reproduces the loading-creep coupling process of rockfills in situ and provides a satisfactory estimate of dam deformation, suggesting the good performance of the unified elastic-plastic-creep model.

Post-construction performance prediction

The further impoundment plan after completion (from the water level 2788 m to normal water level 2865 m) and the post-construction behavior of Lianghekou dam are unavailable. Based on the early impounding process of Lianghekou dam and engineering experience (Hunter and Fell 2003b), the impoundment scheme that the reservoir water level remains at 2788 m in the first 12 months after completion and rises to normal water level from April to June in 2023 is assumed and implemented in this section. Based on Case 3 (SLTP + creep), additional FE analysis is conducted to predict the post-construction deformation of the dam. The dam deformation after completion still grows at a slow rate in Figs. 8–10 and Fig. 11 and a moderate increment in vertical and horizontal displacements can be observed in Figs. 13–15 (green dash-dot line). The sudden increase in horizontal displacement growth rate at C64 and C50 in the downstream shell, as indicated in red circles in Fig. 10, is caused by reservoir water level rising. The post-construction settlement in-

creases along the dam height due to the difference of underlying earthfill thickness (Fig. 13) and hence the maximum is placed at the dam crest in the middle of valley, as shown in Fig. 16a. The predicted distributions of post-construction crest settlement gradient parallel and perpendicular to the dam longitudinal axis are also given in Fig. 16, as well as those in Case 2 (SLTP) for comparison. The simulated results indicate the continuous long-term creep deformation remarkably increases the settlement gradient of dam crest. Some scholars proposed the settlement gradient greater than 1% as an indicator of cracking according to a large number of dam case histories (Zhou et al. 2016; Lin et al. 2017). This work provides an important foundation for further study on dam cracking, especially when considering the collapse behavior of upstream rockfills on wetting.

Conclusions

In this paper, a series of numerical analyses incorporating the loading-creep coupling effect have been performed to reproduce the field observed deformations of Lianghekou CRFD, currently the second-highest CRFD completed in the world. A unified elastic-plastic-creep model applicable to complex loading conditions (including monotonic, cyclic, and creep loading) is adopted. Two sizes of triaxial tests (including 300 and 800 mm in diameter) are conducted on rockfills to model the particle size effect and calibrate the instantaneous elastic-plastic parameters. The time-dependent creep parameters are back-analyzed using in-situ monitoring data. A separation of the instantaneous deformation due to loading and the time-dependent creep deformation has been made by comparison studies of numerical results and measurements. Furthermore, the post-construction performance of the dam is predicted. Some conclusions can be drawn as follows:

- (1) The two suites of calibrations from the triaxial tests on rockfills provide a quantitative representation for the particle size dependence of rockfill behaviors. The underestimation of measurements decreases from 35%–45% to 12%–20% when the instantaneous elastic-plastic

Fig. 15. The settlement distribution along the longitudinal axis of core wall at completion. SLTP, super large-scale triaxial test parameter.

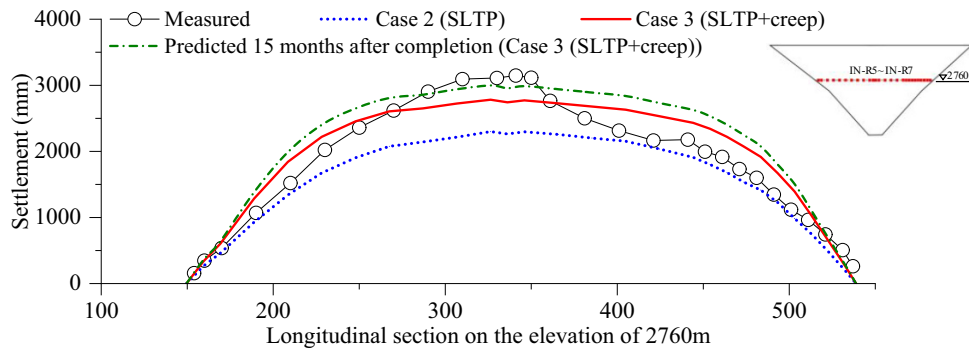
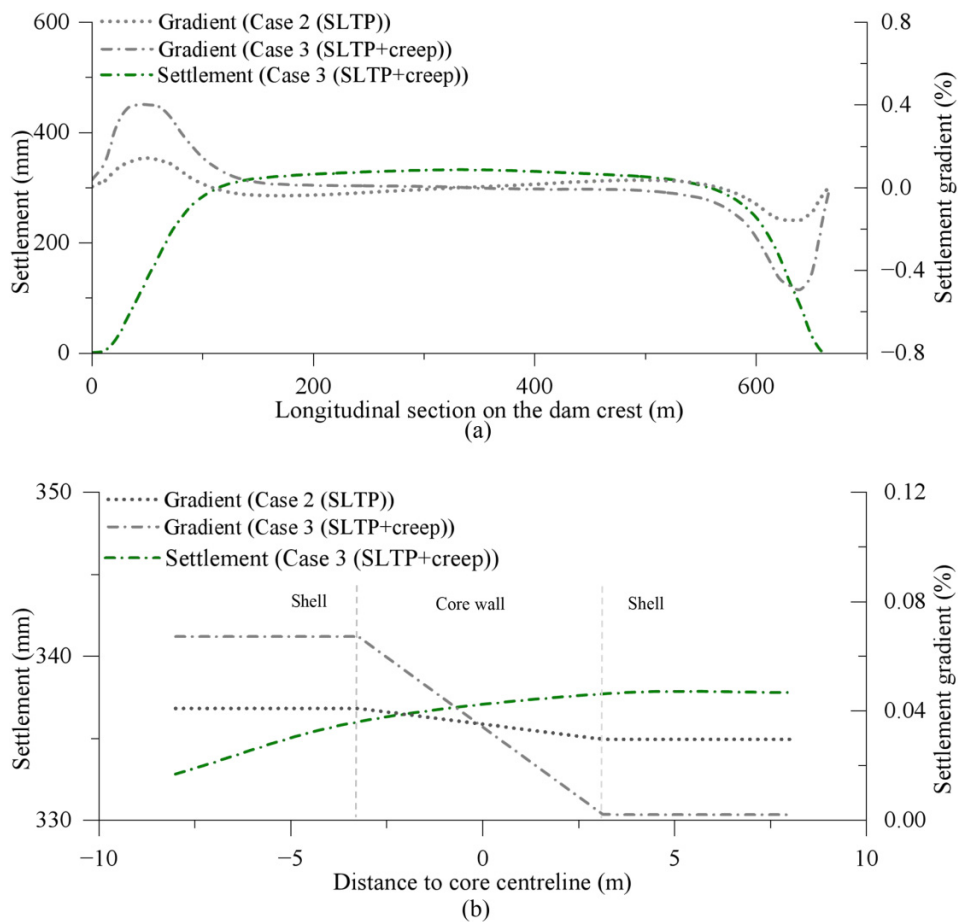


Fig. 16. Crest settlement distributions predicted 15 months after completion: (a) parallel to the dam longitudinal axis and (b) perpendicular to the dam longitudinal axis. SLTP, super large-scale triaxial test parameters.



parameters of rockfills vary from the 300 mm diameter triaxial specimen calibration set to the 800 mm diameter triaxial specimen calibration set. The 800 mm diameter triaxial test provides a reasonable representation for the instantaneous behaviors of prototype rockfills within an acceptable range, especially in the early stage of filling. The underestimation is mainly attributed to the fact that the effect of creep is not included.

(2) The evolution of loading-creep coupling process of dam materials is tracked and exhibited, which allows the explicit separation of the deformation components due to loading and creep in monitoring records. In the early stage of filling, the deformation of rockfills is mainly caused by instantaneous loading because of the elimination of creep effect by large filling load increment. In the later stage, the creep is gradually accumulated in total

deformation with the decrease of filling load increment and the increase of filling period. The time-dependent creep deformation contributes about 8%–15% to total dam deformation at completion. The good agreement between the measured and simulated deformations implies the capability of the model to reproduce the loading-creep behavior of high rockfill dams. The work is helpful for distinguishing instantaneous deformation due to loading from time-dependent creep deformation and provides input for interpreting the behaviors of actual dams.

The underprediction of post-construction settlement in the upstream side of Lianghekou dam crest is mainly attributed to the effect of collapse deformation due to wetting which is not modeled in the present work. In further study, a finer analysis considering the coupled elastic-plastic-creep-wetting behavior of rockfills will be conducted to investigate the dam performance throughout its entire lifecycle.

Acknowledgements

The research work was supported by the National Natural Science Foundation of China (Grant Nos. 52192674, 52079023, 52109114, and 52350393). The authors would like to express their sincerest gratitude for all the financial support.

Article information

History dates

Received: 24 April 2024

Accepted: 10 September 2024

Accepted manuscript online: 3 October 2024

Version of record online: 31 January 2025

Copyright

© 2025 The Author(s). Permission for reuse (free in most cases) can be obtained from [creativecommons.org](https://creativecommons.org/licenses/by/4.0/).

Data availability

The data used during the current study are available from the corresponding author on reasonable request.

Author information

Author ORCIDs

Jingmao Liu <https://orcid.org/0000-0003-3061-345X>

Author contributions

Conceptualization: DZ, JL

Data curation: QJ, FN, WJ

Formal analysis: DZ, JL

Funding acquisition: DZ, JL, FN, KC

Investigation: QJ, FN

Methodology: JL, KC

Project administration: DZ, WJ

Resources: DZ, FN, WJ

Software: DZ, JL, KC

Supervision: DZ, JL

Validation: QJ, JL, FN

Visualization: QJ, FN

Writing – original draft: QJ

Writing – review & editing: QJ, JL

Competing interests

The authors declare there are no competing interests.

References

- Alonso, E.E., Olivella, S., Soriano, A., Pinyol, N.M., and Esteban, F. 2011. Modelling the response of Lechago earth and rockfill dam. *Géotechnique*, **61**(5): 387–407. doi:[10.1680/geot.SIP11.P.013](https://doi.org/10.1680/geot.SIP11.P.013).
- Alonso, E.E., Tapias, M., and Gili, J. 2012. Scale effects in rockfill behavior. *Géotechnique Letters*, **2**(3): 155–160. doi:[10.1680/geolett.12.00025](https://doi.org/10.1680/geolett.12.00025).
- AnhDan, L., Tatsuoka, F., and Koseki, J. 2006. Viscous effects on the stress-strain behavior of gravelly soil in drained triaxial compression. *Geotechnical Testing Journal*, **29**(4): 330–340. doi:[10.1520/GTJ12720](https://doi.org/10.1520/GTJ12720).
- Cetin, H., Laman, M., and Ertunç, A. 2000. Settlement and slaking problems in the world's fourth largest rock-fill dam, the Ataturk Dam in Turkey. *Engineering Geology*, **56**(3–4): 225–242. doi:[10.1016/S0013-7952\(99\)00049-6](https://doi.org/10.1016/S0013-7952(99)00049-6).
- Chen, K., Zou, D., Kong, X., and Yu, X. 2018. An efficient nonlinear octree SBFEM and its application to complicated geotechnical structures. *Computers and Geotechnics*, **96**: 226–245. doi:[10.1016/j.compgeo.2017.10.021](https://doi.org/10.1016/j.compgeo.2017.10.021).
- Chen, K., Zou, D., Liu, J., and Zhuo, Y. 2023. A high-precision formula for mixed-order polygon elements based on SBFEM. *Computers and Geotechnics*, **155**: 105209. doi:[10.1016/j.compgeo.2022.105209](https://doi.org/10.1016/j.compgeo.2022.105209).
- Clements, R.P. 1984. Post-construction deformation of rockfill dams. *Journal of Geotechnical Engineering*, **110**(7): 821–840. doi:[10.1061/\(ASCE\)0733-9410\(1984\)110:7\(821\)](https://doi.org/10.1061/(ASCE)0733-9410(1984)110:7(821)).
- Costa, L.M., and Alonso, E.E. 2009. Predicting the behavior of an earth and rockfill dam under construction. *Journal of Geotechnical and Geoenvironmental Engineering*, **135**(7): 851–862. doi:[10.1061/\(ASCE\)GT.1943-5606.0000058](https://doi.org/10.1061/(ASCE)GT.1943-5606.0000058).
- CS (Chinese Standard). 2019. Standard test methods for soils. SL237. China Water Conservancy and Hydropower Press, Beijing.
- Feda, J. 1992. Creep of soils and related phenomena. Elsevier Science Publishers.
- Fredlund, D.G. 1976. Density and compressibility characteristics of air-water mixtures. *Canadian Geotechnical Journal*, **13**(4): 386–396. doi:[10.1139/t76-040](https://doi.org/10.1139/t76-040).
- Frossard, E., Hu, W., Dano, C., and Hicher, P.Y. 2012. Rockfill shear strength evaluation: a rational method based on size effects. *Géotechnique*, **62**(5): 415–427. doi:[10.1680/geot.10.P.079](https://doi.org/10.1680/geot.10.P.079).
- Fu, Z., Chen, S., Zhong, Q., and Zhang, Y. 2019. Modeling interaction between loading-induced and creep strains of rockfill materials using a hardening elastoplastic constitutive model. *Canadian Geotechnical Journal*, **56**(10): 1380–1394. doi:[10.1139/cgj-2018-0435](https://doi.org/10.1139/cgj-2018-0435).
- Guo, W. 2000. Visco-elastic consolidation subsequent to pile installation. *Computers and Geotechnics*, **26**(2): 113–144.
- Hu, W., Dano, C., Hicher, P.Y., Le Touzo, J.Y., Derkx, F., and Merliot, E. 2011. Effect of sample size on the behavior of granular materials. *Geotechnical Testing Journal*, **34**(3): 186–197. doi:[10.1520/GTJ103095](https://doi.org/10.1520/GTJ103095).
- Hunter, G., and Fell, R. 2003a. Rockfill modulus and settlement of concrete face Rockfill dams. *Journal of Geotechnical and Geoenvironmental Engineering*, **129**(10): 909–917. doi:[10.1061/\(ASCE\)1090-0241\(2003\)129:10\(909\)](https://doi.org/10.1061/(ASCE)1090-0241(2003)129:10(909)).
- Hunter, G., and Fell, R. 2003b. The deformation behaviour of embankment dams. University of New South Wales, School of Civil and Environmental Engineering.
- Jia, Y., Xu, B., Chi, S., Xiang, B., Xiao, D., and Zhou, Y. 2018. Joint back analysis of the creep deformation and wetting deformation parameters of soil used in the Guanyinyan composite dam. *Computers and Geotechnics*, **96**: 167–177. doi:[10.1016/j.compgeo.2017.10.018](https://doi.org/10.1016/j.compgeo.2017.10.018).
- Kong, X., Liu, J., and Zou, D. 2016. Numerical simulation of the separation between concrete face slabs and cushion layer of Zipingpu dam during the Wenchuan earthquake. *Science China Technological Sciences*, **59**: 531–539. doi:[10.1007/s11431-015-5953-6](https://doi.org/10.1007/s11431-015-5953-6).

- Lade, P.V., Liggio, C.D., Jr, and Nam, J. 2009. Strain rate, creep, and stress drop-creep experiments on crushed coral sand. *Journal of Geotechnical and Geoenvironmental Engineering*, **135**(7): 941–953. doi:[10.1061/\(ASCE\)GT.1943-5606.0000067](https://doi.org/10.1061/(ASCE)GT.1943-5606.0000067).
- Li, Y. 2015. The research on the static and dynamic characteristics of gravel clay. Master's thesis. Dalian University of Technology, Dalian, China.
- Lin, D., Zhu, X., Yan, M., Chen, X., and Ying, J. 2017. Cause analysis of crest cracking of Pubugou Rockfill Dam with a central gravelly soil core during first reservoir impounding. *Chinese Water Power*, **43**(10): 50–61.
- Ling, H.I., and Liu, H. 2003. Pressure-level dependency and densification behavior of sand through generalized plasticity model. *Journal of Engineering Mechanics*, **129**(8): 851–860. doi:[10.1061/\(ASCE\)0733-9399\(2003\)129:8\(851\)](https://doi.org/10.1061/(ASCE)0733-9399(2003)129:8(851)).
- Ling, H.I., and Yang, S. 2006. Unified sand model based on the critical state and generalized plasticity. *Journal of Engineering Mechanics*, **132**(12): 1380–1391. doi:[10.1061/\(ASCE\)0733-9399\(2006\)132:12\(1380\)](https://doi.org/10.1061/(ASCE)0733-9399(2006)132:12(1380)).
- Liu, J., Zou, D., Ning, F., and Kong, X. 2023. A unified constitutive model for instantaneous elastic-plastic and time-dependent creep behavior of gravelly soils under complex loading. *Canadian Geotechnical Journal*, **60**(11): 1613–1628.
- Liu, X., Zou, D., Liu, J., and Zheng, B. 2021. Predicting the small strain shear modulus of coarse-grained soils. *Soil Dynamics and Earthquake Engineering*, **141**: 106468. doi:[10.1016/j.soildyn.2020.106468](https://doi.org/10.1016/j.soildyn.2020.106468).
- Lollino, P., Cotecchia, F., Zdravkovic, L., and Potts, D.M. 2005. Numerical analysis and monitoring of pappadai dam. *Canadian Geotechnical Journal*, **42**(6): 1631–1643. doi:[10.1139/t05-079](https://doi.org/10.1139/t05-079).
- Ma, S.Y.A., and May, I.M. 1986. The Newton-Raphson method used in the non-linear analysis of concrete structures. *Computers & Structures*, **24**(2): 177–185. doi:[10.1016/0045-7949\(86\)90277-4](https://doi.org/10.1016/0045-7949(86)90277-4).
- Mahinroosta, R., Alizadeh, A., and Gatmiri, B. 2015. Simulation of collapse settlement of first filling in a high rockfill dam. *Engineering Geology*, **187**: 32–44. doi:[10.1016/j.enggeo.2014.12.013](https://doi.org/10.1016/j.enggeo.2014.12.013).
- Mahinroosta, R., and Alizadeh, A. 2012. Simulation of collapse settlement in rockfill material due to saturation. *International Journal of Civil Engineering*, **10**(2): 93–99.
- Marachi, N. 1969. Strength and deformation characteristics of rockfill materials. PhD thesis. University of California, Berkeley.
- Maranha das Neves, E. 1991. Advances in rockfill structures. Proc. NATO Advanced Study Institute on Advances in Rockfill Structures.
- Marsal, R.J. 1967. Large scale testing of rockfill materials. *Journal of the Soil Mechanics and Foundations Division*, **93**(2): 27–43. doi:[10.1061/JSEFAQ.0000958](https://doi.org/10.1061/JSEFAQ.0000958).
- Marsal, R.J. 1973. Mechanical properties of rockfill. Publication of: Wiley (John) and Sons, Incorporated.
- Marschi, N.D., Chan, C.K., and Seed, H.B. 1972. Evaluation of properties of rockfill materials. *Journal of the Soil Mechanics and Foundations Division*, **98**(1): 95–114. doi:[10.1061/JSEFAQ.0001735](https://doi.org/10.1061/JSEFAQ.0001735).
- Naylor, D. 1974. Stresses in nearly incompressible materials by finite elements with application to the calculation of excess pore pressures. *International Journal for Numerical Methods in Engineering*, **8**(3): 443–460. doi:[10.1002/nme.1620080302](https://doi.org/10.1002/nme.1620080302).
- Naylor, D.J., Maranhã, J.R., Neves, E.M.D., and Pinto, A.V. 1997. A back-analysis of Beliche Dam. *Géotechnique*, **47**(2): 221–233. doi:[10.1680/geot.1997.47.2.221](https://doi.org/10.1680/geot.1997.47.2.221).
- Ning, F. 2022. Research on the scale effect of coarse grained materials based on super large triaxial apparatus. PhD thesis. Dalian University of Technology, Dalian, China.
- Ohkami, T., and Swoboda, G. 1999. Parameter identification of viscoelastic materials. *Computers and Geotechnics*, **24**(4): 279–295. doi:[10.1016/S0266-352X\(99\)00011-7](https://doi.org/10.1016/S0266-352X(99)00011-7).
- Oldecop, L.A., and Alonso, E.E. 2007. Theoretical investigation of the time-dependent behaviour of rockfill. *Géotechnique*, **57**(3): 289–301. doi:[10.1680/geot.2007.57.3.289](https://doi.org/10.1680/geot.2007.57.3.289).
- Ovalle, C., Frossard, E., Dano, C., Hu, W., Maiolino, S., and Hicher, P.Y. 2014. The effect of size on the strength of coarse rock aggregates and large rockfill samples through experimental data. *Acta Mechanica*, **225**: 2199–2216. doi:[10.1007/s00707-014-1127-z](https://doi.org/10.1007/s00707-014-1127-z).
- Seo, M.W., Ha, I.S., Kim, Y.S., and Olson, S.M. 2009. Behavior of concrete-faced rockfill dams during initial impoundment. *Journal of Geotechnical and Geoenvironmental Engineering*, **135**(8): 1070–1081. doi:[10.1061/\(ASCE\)GT.1943-5606.0000021](https://doi.org/10.1061/(ASCE)GT.1943-5606.0000021).
- Sowers, G.F. 1965. Compressibility of broken rock and the settlement of rockfills. In *Proceedings of the 6th International Conference on Soil Mechanics and Foundation Engineering*, Montreal, Canada. pp. 561–565.
- Varadarajan, A., Sharma, K.G., Abbas, S.M., and Dhawan, A.K. 2006. Constitutive model for rockfill materials and determination of material constants. *International Journal of Geomechanics*, **6**(4): 226–237. doi:[10.1061/\(ASCE\)1532-3641\(2006\)6:4\(226\)](https://doi.org/10.1061/(ASCE)1532-3641(2006)6:4(226)).
- Wen, L., Chai, J., Xu, Z., Qin, Y., and Li, Y. 2017. Monitoring and numerical analysis of behaviour of Miaojiba concrete-face rockfill dam built on river gravel foundation in China. *Computers and Geotechnics*, **85**: 230–248. doi:[10.1016/j.compgeo.2016.12.018](https://doi.org/10.1016/j.compgeo.2016.12.018).
- Wen, L., Chai, J., Xu, Z., Qin, Y., and Li, Y. 2018. A statistical review of the behaviour of concrete-face rockfill dams based on case histories. *Géotechnique*, **68**(9): 749–771. doi:[10.1680/jgeot.17.P.095](https://doi.org/10.1680/jgeot.17.P.095).
- Xiao, Y., and Liu, H. 2017. Elastoplastic constitutive model for rockfill materials considering particle breakage. *International Journal of Geomechanics*, **17**(1): 04016041. doi:[10.1061/\(ASCE\)GM.1943-5622.0000681](https://doi.org/10.1061/(ASCE)GM.1943-5622.0000681).
- Xiao, Y., Liu, H., Chen, Y., Jiang, J., and Zhang, W. 2015. State-dependent constitutive model for rockfill materials. *International Journal of Geomechanics*, **15**(5): 04014075. doi:[10.1061/\(ASCE\)GM.1943-5622.0000421](https://doi.org/10.1061/(ASCE)GM.1943-5622.0000421).
- Xiao, Y., Meng, M., Daouadji, A., Chen, Q., Wu, Z., and Jiang, X. 2020a. Effects of particle size on crushing and deformation behaviors of rockfill materials. *Geoscience Frontiers*, **11**(2): 375–388. doi:[10.1016/j.gsf.2018.10.010](https://doi.org/10.1016/j.gsf.2018.10.010).
- Xiao, Y., Sun, Z., Stuedlein, A.W., Wang, C., Wu, Z., and Zhang, Z. 2020b. Bounding surface plasticity model for stress-strain and grain-crushing behaviors of rockfill materials. *Geoscience Frontiers*, **11**(2): 495–510. doi:[10.1016/j.gsf.2019.06.010](https://doi.org/10.1016/j.gsf.2019.06.010).
- Xu, B., Zou, D., and Liu, H. 2012. Three-dimensional simulation of the construction process of the Zipingpu concrete face rockfill dam based on a generalized plasticity model. *Computers and Geotechnics*, **43**: 143–154. doi:[10.1016/j.compgeo.2012.03.002](https://doi.org/10.1016/j.compgeo.2012.03.002).
- Xu, H., Zou, D., Kong, X., and Hu, Z. 2016. Study on the effects of hydrodynamic pressure on the dynamic stresses in slabs of high CFRD based on the scaled boundary finite-element method. *Soil Dynamics and Earthquake Engineering*, **88**: 223–236. doi:[10.1016/j.soildyn.2016.06.003](https://doi.org/10.1016/j.soildyn.2016.06.003).
- Yang, Z., Wang, Z., Zhang, L., Zhou, R., and Xing, N. 2001. Back-analysis of viscoelastic displacements in a soft rock road tunnel. *International Journal of Rock Mechanics and Mining Sciences*, **38**(3): 331–341.
- Yao, Y., and Fang, Y. 2020. Negative creep of soils. *Canadian Geotechnical Journal*, **57**(1): 1–16. doi:[10.1139/cgj-2018-0624](https://doi.org/10.1139/cgj-2018-0624).
- Zhang, B., Chen, T., Peng, C., Qian, X., and Jie, Y. 2017. Experimental study on loading-creep coupling effect in rockfill material. *International Journal of Geomechanics*, **17**(9): 04017059. doi:[10.1061/\(ASCE\)GM.1943-5622.0000938](https://doi.org/10.1061/(ASCE)GM.1943-5622.0000938).
- Zhang, B., Wang, J., and Shi, R. 2004. Time-dependent deformation in high concrete-faced rockfill dam and separation between concrete face slab and cushion layer. *Computers and Geotechnics*, **31**(7): 559–573. doi:[10.1016/j.compgeo.2004.07.004](https://doi.org/10.1016/j.compgeo.2004.07.004).
- Zhou, W., Hua, J., Chang, X., and Zhou, C. 2011. Settlement analysis of the Shuibuya concrete-face rockfill dam. *Computers and Geotechnics*, **38**(2): 269–280. doi:[10.1016/j.compgeo.2010.10.004](https://doi.org/10.1016/j.compgeo.2010.10.004).
- Zhou, W., Li, S.L., Ma, G., Chang, X.L., Cheng, Y.G., and Ma, X. 2016. Assessment of the crest cracks of the Pubugou rockfill dam based on parameters back analysis. *Geomechanics and Engineering*, **11**(4): 571–585. doi:[10.12989/gae.2016.11.4.571](https://doi.org/10.12989/gae.2016.11.4.571).
- Zhou, X., Ma, G., and Zhang, Y. 2018. Grain size and time effect on the deformation of rockfill dams: a case study on the Shuibuya CFRD. *Géotechnique*, **69**: 606–619. doi:[10.1680/jgeot.17.p.299](https://doi.org/10.1680/jgeot.17.p.299).
- Zhu, Y. 2017. Study on rockfill rheological properties and pre-settlement control measures of high CFRD. PhD thesis. Dalian University of Technology, Dalian, China.
- Zou, D., Jiang, Q., Liu, J., Zhu, X., and Jing, W. 2022. Characteristics and mechanism of inhomogeneous pore pressure of core wall in super-high rockfill dam. *Chinese Journal of Hydraulic Engineering*, **53**(12): 1467–1475.
- Zou, D., Kong, X., and Xu, B. 2005. User manual for geotechnical dynamic nonlinear analysis. Institute of earthquake engineering. Dalian University of Technology, Dalian.

Zou, D., Xu, B., Kong, X., Liu, H., and Zhou, Y. 2013. Numerical simulation of the seismic response of the Zipingpu concrete face rockfill dam during the Wenchuan earthquake based on a generalized plasticity model. *Computers and Geotechnics*, **49**: 111–122. doi:[10.1016/j.compgeo.2012.10.010](https://doi.org/10.1016/j.compgeo.2012.10.010).

Zuo, Y., Zhao, N., and Zhou, Y. 2020. Experimental study on strength and deformation characteristics of gravelly soil core materials. *Chinese Journal of Geotechnical Engineering*, **42**(S1): 100–104.